Estimation of cardiac motion in cine-MRI sequences by correlation transform optical flow of monogenic features distance

Bin Gao, Wanyu Liu, Liang Wang, Zhengjun Liu, Pierre Croisille, Philippe Delachartre, Patrick Clarysse

Estimation of cardiac motion in cine-MRI sequences by correlation transform optical flow of monogenic features distance

Bin Gao[1,2], Wanyu Liu[1], Liang Wang[3], Zhengjun Liu[1], Pierre Croisille[3,4], Philippe Delachartre[3] and Patrick Clarysse[3]

[1] Metislab, LIA CNRS, Harbin Institute of Technology, Harbin 150001, People's Republic of China

[2] College of information science and technology, Heilongjiang University, Harbin 150080, People's Republic of China

[3] Univ Lyon, INSA-Lyon, Université Lyon 1, Université Jean Monnet, CNRS, Inserm, CREATIS UMR 5220, U1206, F-69621, Lyon, France

[4] Department of Radiology, University Hospital of Saint-Etienne, Université Jean-Monnet, Saint-Etienne, France

E-mail: liu.wanyu@gmail.com

Abstract

Cine-MRI is widely used for the analysis of cardiac function in clinical routine, because of its high soft tissue contrast and relatively short acquisition time in comparison with other cardiac MRI techniques. The gray level distribution in cardiac cine-MRI is relatively homogenous within the myocardium, and can therefore make motion quantification difficult. To ensure that the motion estimation problem is well posed, more image features have to be considered. This work is inspired by a method previously developed for color image processing. The monogenic signal provides a framework to estimate the local phase, orientation, and amplitude, of an image, three features which locally characterize the 2D intensity profile. The independent monogenic features are combined into a 3D matrix for motion estimation. To improve motion estimation accuracy, we chose the zero-mean normalized cross-correlation as a matching measure, and implemented a bilateral filter for denoising and edge-preservation. The monogenic features distance is used *in lieu* of the color space distance in the bilateral filter. Results obtained from four realistic simulated sequences outperformed two other state of the art methods even in the presence of noise. The motion estimation errors (end point error) using our proposed method were reduced by about 20% in comparison with those obtained by the other tested methods. The new methodology was evaluated on four clinical

sequences from patients presenting with cardiac motion dysfunctions and one healthy volunteer. The derived strain fields were analyzed favorably in their ability to identify myocardial regions with impaired motion.

Keywords: cardiac motion estimation, cine-magnetic resonance imaging (cine-MRI), correlation transform, bilateral filtering, monogenic features, optical flow

(Some figures may appear in colour only in the online journal)

1. Introduction

The mechanical status of the pathological heart can be assessed by cardiac motion and strains measurements, which may be evaluated using cardiac imaging (D'Hooge *et al* 2000, Wang and Amini 2012, Wang *et al* 2015). Cardiac magnetic resonance imaging (MRI) has become a standard diagnostic technique for the noninvasive assessment of cardiac function in the diagnosis of cardiovascular disease, as it allows for the measurement of both anatomical and functional myocardial parameters (White *et al* 1996, Axel *et al* 2005). Cardiac function measurement is important for the evaluation of treatments in patients with heart failure; however, some of the measurements currently used, such as ejection fraction and segmental myocardial thickening, remain global and imprecise. Accurate local quantification of the motion would certainly allow a much more accurate characterization of the myocardial function (Werys *et al* 2013).

Although tagged-MRI (T-MRI; Zerhouni *et al* 1988, Axel and Dougherty 1989) is considered the reference method for myocardial motion quantification, it is not part of the conventional imaging protocol for LV function assessment. On the contrary, cine-MRI has been acquired routinely for years. Therefore, accurate regional strain assessment from cine-MRI would be extremely useful.

A few methods have been proposed to date for the quantification of myocardial motion based on cine-MRI (in a significantly lower number than for T-MRI). The main difficulty as compared to T-MRI is the lack of an intensity distribution structure within the myocardium (rather an homogeneous intensity distribution), which limits natural landmarks that would ease the temporal correspondence search. Basically, optical flow- (Amartu and Vesselle 1993, Xavier *et al* 2012) or registration-based methods (Lamacie *et al* 2016) and recent feature tracking (FT) methods (Hor *et al* 2010) have been proposed.

The FT method was initially introduced in cardiac ultrasound imaging and further applied to cardiac MRI (Hor *et al* 2010). It tracks selected endocardial contour points along 1D profiles by constructing an echographic T-mode-like image. Reasonable agreement with T-MRI for global circumferential strain values has been observed (Cowan *et al* 2015), but the limits of agreement were much wider for other strains (Augustine *et al* 2013). It should be noted that motion measurements are sparser with this type of approach than with optical flow- or registration-based methods. The pertinence of FT-derived strains continues to be debated in the literature (Augustine *et al* 2013, Wu *et al* 2014, Kuetting *et al* 2015).

Until now, there has been no consensus on a method for the quantification of the regional cardiac function from cine-MRI acquisitions. The present work introduces a new optical flow- and monogenic signal-based method for this purpose, which was originally proposed in a different context and has been shown to provide accurate quantification of myocardial displacement and strains in our experiments on both simulated and clinical data as compared to other methods.

Optical flow estimation has gained a lot of attention because of its importance in video processing. It has also been experimented for cardiac motion analysis (Amartur and Vesselle 1993, Gorce *et al* 1997). The monogenic signal was introduced by Felsberg and Sommer (2001) and Felsberg (2007), to extend the analytic signal concept to multiple dimensions. In image processing situations where the traditional pixel intensity cannot be considered a reliable feature, the monogenic signal is a possible solution for a number of problematic issues. The monogenic phase has also been proposed for use in motion estimation tasks (Felsberg and Sommer 2001, Felsberg 2007). Due to the lack of image-texture and landmarks within the myocardium in cine-MR images, the phase information alone is insufficient for cardiac motion estimation. To introduce more features, we have constructed a 3D matrix combining local amplitude, local phase, and local orientation, which is used as the input image to an optical flow based approach.

Zero-mean normalized cross-correlation (ZNCC; Di Stefano *et al* 2005, Drulea and Nedevschi 2013) of two signals, is the sum of the squared difference (SSD) of the distance between the correlation transforms of the signals (Drulea and Nedevschi 2013). In motion estimation, the ZNCC model is employed between the correlation transform of consecutive images. After this transformation, a traditional optical flow framework can be adopted.

Through a nonlinear combination of neighboring image values, bilateral filtering (Tomasi and Manduchi 1998, Lin *et al* 2010) can smooth images while preserving edges. The method is non-iterative, local and simple. It is based on both geometric closeness, and image similarity features, and gives preference to close rather than distant values, in both the transform and spatial domains. In contrast with filters that operate separately on different features of an image, a bilateral filter can enforce the perceptual metric underlying the monogenic features space. Averaged or weighted summing of the combined data can provide more features for motion estimation, and therefore lead to more reliable results.

The methodological contribution of this paper is to construct a synthesis matrix of monogenic features as a *pseudo-color* image to be input into an optical flow operator. The ability of the proposed method to accurately quantify myocardial motion in 2D cine-MRI sequences is evaluated and compared with similar methods, using both simulated and clinical image sequences.

This paper is organized as follows. Section 2 details the computation of monogenic features: ZNCC, the bilateral filter, and the projected proximal point algorithm (PPPA). These are outlined as the methodologies involved in the optical flow approach based on correlation transform. Section 3 introduces the generation of simulated data, region masks, and evaluation of the methods with simulated sequences. Experiments on clinical data are described in section 4, and then discussed in section 5.

2. Methodology

Motion estimation methods generally estimate a displacement field between two consecutive images of a temporal sequence. Due to the textureless appearance of the myocardium in cine-MRI, more features should be introduced into the optical flow framework. Monogenic phases were previously proposed for driving an optical flow method (Felsberg 2007). However, over nearly homogenous regions of the image, phases may be insufficient to estimate the local motion. The work in this study is inspired by the work of Drulea and Nedevschi (2013) on color image processing, where the RGB components of the color image are considered as three complementary images. In this study, the three monogenic features provided by the 2D analytic signal of a cine MR image, namely the local amplitude, phase, and orientation,

are combined into a pseudo-color image, and input into the optical flow equations. ZNCC is employed as a matching measure for the data fidelity term. Bilateral filtering of weighted coefficients within a local window is applied for data regularization. The filtering operation with spatial averaging is nonlinear, and avoids smoothing across edges. A coarse-to-fine warping strategy, which allows for the detection of substantial motion, is implemented in the filtering operation. A minimization scheme based on the PPPA is employed to optimize the final result (Chambolle and Pock 2011, He and Yuan 2012).

2.1. Pseudo color matrix of the monogenic signal features

The monogenic model can be considered as a 2D generalization of an analytic signal. The information included in the monogenic signal is orthogonally decomposed into local amplitude, local orientation, and local phase (Felsberg 2007); therefore, each presentation is also preserved with respect to energetic, geometric, and structural information (Felsberg and Sommer 2001). The three parts are regarded as the three components of a 'pseudo color' image.

In the definition of a monogenic signal, the amplitude, phase, and orientation are computed from the responses to three 2D spherical quadrature filters (SQFs; Felsberg and Sommer 2001, Alessandrini *et al* 2013). The SQFs consist of one even rotation invariant bandpass filter $h_e(\mathbf{x})$, and two odd bandpass filters $h_{o1}(\mathbf{x})$, and $h_{o2}(\mathbf{x})$, where $\mathbf{x} = (x, y)$ designates the Cartesian coordinates. These two filters represent quadrature phase shifting operations in the two orthogonal directions. The Riesz transform acts as a 2D equivalent of the Hilbert transform. The odd filters are calculated from the Riesz transform of the even filter (Felsberg and Sommer 2001, Felsberg 2007). In the frequency domain,

$$H_{o1}(\boldsymbol{\omega}) = -\frac{\mathrm{i}\omega_x}{|\boldsymbol{\omega}|} \cdot H_e(\boldsymbol{\omega}),\ H_{o2}(\boldsymbol{\omega}) = -\frac{\mathrm{i}\omega_y}{|\boldsymbol{\omega}|} \cdot H_e(\boldsymbol{\omega}), \tag{1}$$

where $\boldsymbol{\omega} = [\omega_x, \omega_y]^T$ is the normalized angular frequency. Several SQF families have been employed in previous studies (Felsberg and Sommer 2001). A highpass filter determines the details of the image; a Butterworth filter is used here, in the modulation of the frequency domain (Yang *et al* 2015), and is expressed as

$$H_e(\boldsymbol{\omega}) = \frac{1}{1 + (\omega_c / \boldsymbol{\omega})^{2n}}, \tag{2}$$

where ω_c and n are the cutoff frequency and order respectively. From the three filter responses, the monogenic phase $\varphi(x)$, orientation $\theta(x)$, and amplitude $A(x)$, of an image I (Felsberg 2007), can be obtained as

$$A(\mathbf{x}) = \sqrt{q_1(\mathbf{x})^2 + q_2(\mathbf{x})^2 + p(x)^2};\ \theta(\mathbf{x}) = \arctan\left(\frac{q_2(\mathbf{x})}{q_1(\mathbf{x})}\right), \tag{3}$$

$$\mathrm{Im}(\mathbf{x}) = [A(\mathbf{x}), \varphi(\mathbf{x}), \theta(\mathbf{x})], \tag{4}$$

where $p(\mathbf{x}) = (I^{**}h_e)(\mathbf{x})$, $q_1(\mathbf{x}) = (I^{**}h_{o1})(\mathbf{x})$, $q_2(\mathbf{x}) = (I^{**}h_{o2})(\mathbf{x})$, $\mathbf{q}(\mathbf{x}) = [\ q_1\ \mathbf{x}), q_2(\mathbf{x})]^T$, and the symbol '$**$' denotes a 2D convolution. Although $\varphi(x)$, $\theta(x)$ and $A(x)$ have different values, we normalize each of them between 0 and 255 from minimum to maximum. The three normalized results are considered, respectively, as red, blue, and green channels combined into a composite pseudo color image $\mathrm{Im}(\mathbf{x})$, as shown in figure 1 and equation (4).

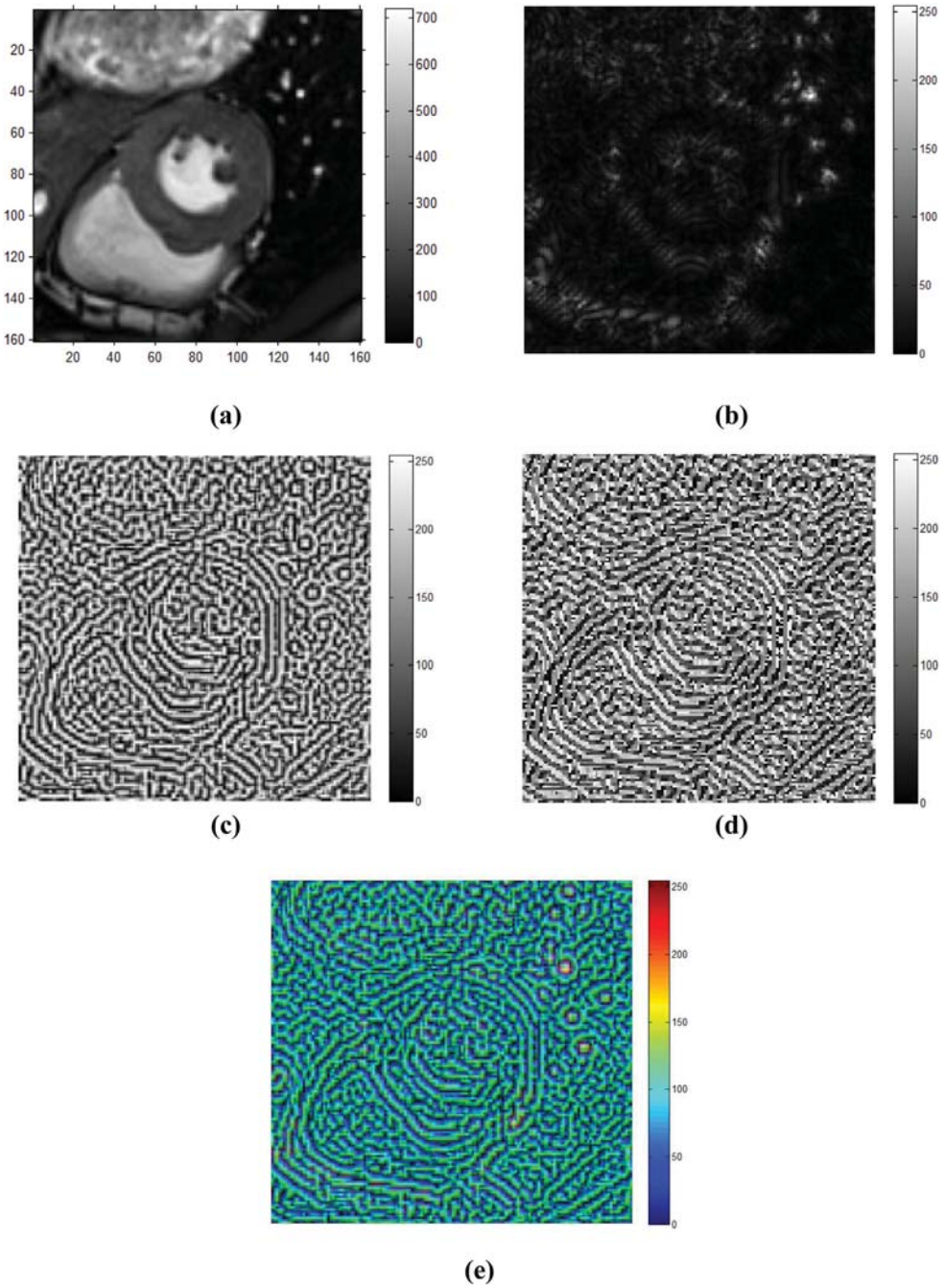

Figure 1. 2D monogenic signal and composite pseudo color image: (a) original cine-MRI image, (b)–(d) images of local amplitude, phase, and orientation, and (e) composite pseudo color image.

2.2. ZNCC based optical flow

Horn and Schunck proposed an approach to estimate optical flow within a variational scheme, using the minimization of a function that included a data fidelity term E_{d}, and a smoothness term E_{r} (Horn and Schunck 1981). The data fidelity term measures the degree of similarity between two pixels (or patches) in terms of intensity, color, or some other measure. The smoothness term actually is the regularity of the solution. The solution results from an optimization, which is often expressed as the minimization of an energy combining the two terms: $E(V) = E_{\mathrm{d}}(V) + \varepsilon \cdot E_{\mathrm{r}}(V)$, where ε controls the regularization (Horn and Schunck 1981). The two unknowns are the velocity components $[u, v] = V$ in the horizontal and vertical directions.

The matching criterion used for the data term in dense optical flow estimation, is commonly defined as the pixel intensities and/or the intensity gradients conserved during motion. Other criteria may be desirable to increase the accuracy and robustness.

The correlation criterion quantifies the similarity between the reference and target patches. One basic method for signal matching is to calculate the sum of the SSD between two signals in a window (Okutomi and Kanade 1992). In SSD intensity matching, robustness against noise is increased. The SSD is expressed as

$$\mathrm{SSD}(R, T) = \sum_{j \in N} (R_j - T_j)^2, \tag{5}$$

where R and T are two patches having the same dimension. The index j addresses the N pixel locations within the patch.

The ZNCC can improve the patch pairing accuracy, as it is known to be robust to noise and illumination changes. It can also provide better fidelity in textureless regions. The ZNCC operator is defined as the correlation transform

$$\mathrm{ZNCC}(R, T) = \frac{1}{|N|} \cdot \frac{\langle R - \mu_R, T - \mu_T \rangle}{\sigma_R \cdot \sigma_T}, \tag{6}$$

where $|N|$ represents the cardinal number of the squared patches R and T. The values μ_X and σ_X are the mean and standard deviation of $X \in \{R, T\}$. The symbol $\langle , \rangle$ represents the standard dot product. If R and T are identical, this measure takes the value of 1. The best match for the patches R and T maximizes the function $\mathrm{ZNCC}(R, T)$.

The ZNCC of two signals is in fact the SSD distance between their correlation transforms (Drulea and Nedevschi 2013). We therefore consider the difference of the correlation transform descriptor C as the ZNCC measurement used in the optical flow method.

As in the methods of Drulea and Nedevschi (2013), the image I is first converted to C by the following correlation transform:

$$C(i) = \left[\frac{I(j) - \mu(i)}{\sigma(i)} \right], j \in N_i, \tag{7}$$

where $\mu(i)$ and $\sigma(i)$ are the mean value and standard deviation of the block N_i, where N_i contains the indices around pixel i.

Let I_1, I_2 be two consecutive images of a sequence. Given the image I_1 and the warped second image I_2, their descriptors C_1, C_2 (pixel-wise; equation (7)) are matched through equation (7). The displacement $\mathrm{d}V$, should satisfy the equation $C_2(i + \mathrm{d}V_i) = C_1(i)$, which translates the invariance in C, instead of the intensity used in the classical optical flow method.

On the basis of this assumption, we can define the total matching error (or data error) by accumulating the distances between descriptors:

$$E_{\mathrm{d}}(\mathrm{d}V) = \sum_{i\in\Omega} \frac{1}{|N_i|} \|C_2(i + \mathrm{d}V_i) - C_1(i)\|^2, \tag{8}$$

where Ω is the whole $m \times n$ image. Each pixel has a 2D index $i \in \Omega$, and its neighborhood is denoted as N_i. The two adjacent images can directly take measured data as arguments. However, the values at these locations are computed using interpolation for precise displacement estimation. The displacement $\mathrm{d}V_i$, denotes the flow at location i in the image.

The residual at location i and component index k are evaluated. The total matching energy error (Drulea and Nedevschi 2013) is defined as the following convex function

$$E_{\mathrm{d}}(\mathrm{d}V) = \sum_{i\in\Omega} \sum_{k} [C_{\mathrm{t}}(i,k) + \nabla C(i,k) \cdot (\mathrm{d}V_i)]^2 \ . \tag{9}$$

where $C(i,k)$ is the descriptor $C(i)$ in the different components of the pseudo color image, and $k = 1$–3 is the index of the components of the pseudo color image corresponding to the monogenic components. The term $C_{\mathrm{t}}(i,k) = C_2(i,k) - C_1(i,k)$ represents the temporal gradient approximation and $\nabla C(i,k) = (\nabla C_1(i,k) + \nabla C_2(i,k))/2$ is used as a blend derivative (Wedel *et al* 2009). There are therefore two main steps to establish the feature similarity of two images: (1) construction of the descriptors of image characteristics C (equation (7)), and (2) estimation of the distance expressing motion through the minimization of equation (9).

2.3. Data regularization with bilateral filtering

Bilateral filtering is a robust edge-preserving operation proposed by Tomasi and Manduchi (1998). The operator is nonlinear, and can smooth a signal while preserving strong edges. It has been used for many issues in computer vision and graphics. In this study, bilateral filtering is adopted to reduce over-smoothing across region edges. Two types of bilateral filters (Tomasi and Manduchi 1998, Zhang and Gunturk 2008, Lin *et al* 2010, Drulea and Nedevschi 2013) have been introduced: a spatial filter, and a transform domain filter. These are determined by the computed distance between the center pixel and its neighbors. The two filter kernels are traditionally based on a Gaussian distribution weighting. In addition, the weight depends on the difference of the monogenic features between a pixel and the center of the corresponding block.

While spatial filtering merely spatially smooths the monogenic feature map of an image, filtering in both spatial and frequency domains can enrich the features of an image. This is especially the case if the bilateral filter is just a synthesis method. The filtering can be applied to 2D data for the determination of distance. Here, the bilateral filter is applied to monogenic features, and the coefficient of bilateral filtering is expressed as:

$$\mathrm{BF}_{i,s} = \mathrm{e}^{-\left(\frac{\Delta_{\mathrm{m}}(i,s)}{2\sigma_{\mathrm{m}}^2} + \frac{\Delta_{\mathrm{d}}(i,s)}{2\sigma_{\mathrm{d}}^2}\right)}, \tag{10}$$

where $\Delta_{\mathrm{m}}(i,s)$ represents the distance between the monogenic features of the pixels i and s computed in the monogenic features space. The function $\Delta_{\mathrm{d}}(i,s) = \|i,s\|^2$ is simply the Euclidean distance between two pixels. The parameters σ_{d} and σ_{m} control the respective weight of the two distance measurements. The pixel s belongs to the neighborhood N_i of the pixel at location i.

In this work, bilateral filtering is used for the regularization of displacement fields. The motion estimation is based on the assumption of the spatial coherence of the monogenic features of the underlying image. The pixels representing rigid objects should have almost the same velocity. The deviation from this constancy assumption is evaluated by the following error metrics:

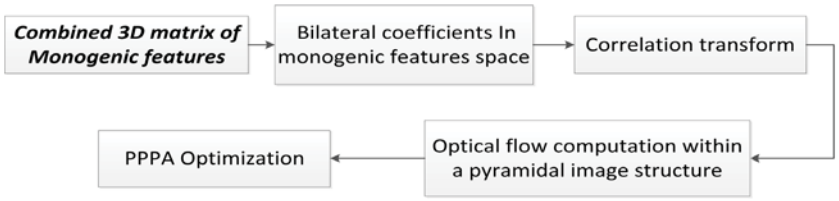

Figure 2. Flowchart of the proposed motion estimation method.

$$\begin{aligned} E_{\text{regular}}(i) &= \sum_{s\in N_i} \text{BF}_{i,s} \cdot \|V_s - V_i\|_1 \\ &= \sum_{s\in N_i} \left\{ \text{BF}_{i,s} \cdot |u_s - u_i| + \text{BF}_{i,s} \cdot |v_s - v_i| \right\}, \end{aligned} \tag{11}$$

where $\text{BF}_{i,s}$ measures how likely the pixels i and s belong to the same moving object. $\text{BF}_{i,s}$ tends towards zero when the monogenic features in i and s are close to each other. Therefore, the regularity metric E_{regular} combines the velocity differences at locations sharing the same monogenic signature.

For the whole image, the total smoothness error is calculated as:

$$E_{\text{r}}(V) = \sum_{i\in\Omega} \sum_{s\in N_i} \text{BF}_{i,s} \cdot \|V_s - V_i\|_1. \tag{12}$$

Like most variational approaches, the presented model relies on the first-order Taylor series expansion of the data matching term (equation (9)), but based on the image descriptor C. It is also integrated into a coarse-to-fine strategy in order to deal with large displacements (see figure 2). Bilinear interpolation is used as a downsampling operator to build the pyramids from the finest (original image) to the coarsest level. The bilateral coefficients and the correlation transform for optical flow are computed for the two pyramids. Bicubic interpolation is used as the upsampling operator to project the flow from the current level to the finer one (coarse-to-fine). We also tried bicubic downsampling to build the pyramid, but we found it affected the bilateral coefficients (Drulea and Nedevschi 2013). In our experiments, 0.3 is employed as the pyramid factor.

2.4. Algorithm optimization and synthesized optical flow scheme

The considered optical flow model includes a fast and parallelizable minimization procedure, based on the PPPA (Drulea and Nedevschi 2013). The strength of this model will be confirmed experimentally. PPPA is notably used for solving variational inequalities (Drulea and Nedevschi 2013), and the method can be seen as a regularization technique for the ill-posed motion estimation problem. In this study, an improved version of PPPA (Xia and Huang 2011) for solving a class of generalized variational inequalities, has been considered for optimization of the evaluated displacement. The discretized optical flow can be adapted to a convex–concave problem. The proximal point strategy (Chambolle and Pock 2011) implies the min-maximization theory of convex–concave functions. It results in a system of linear equations, which are simple to solve (Drulea and Nedevschi 2013). The workflow for the proposed motion estimation method, based on the operators detailed above, is illustrated in figure 2.

2.5. Lagrangian displacement and strain estimation

Identification, localization, and grading of abnormal cardiac regions are of high clinical value. Myocardial strain patterns from MRI can be used to identify and locate regional abnormalities in cardiac function in human subjects (Qian *et al* 2011, Sadeghpour 2013). A methodology to obtain the Green–Lagrange strain tensor, with end-diastole taken as the reference state, is briefly outlined below.

The Lagrangian motion field (Oubel *et al* 2012, Wang *et al* 2015) represents the spatio-temporal displacement of sampled material points in a reference frame (end-diastole time point). This spatio-temporal Lagrangian displacement field $[d_{Lx}(x, y), d_{Ly}(x, y)]$ can be recovered through the accumulation of the Eulerian motion field $[d_{Ex}(x, y), d_{Ey}(x, y)]$ between every two successive frames. Given a motion field between time t and $t + 1$, the Lagrangian motion field $[d_{Lx}(x, y, t + 1), d_{Ly}(x, y, t + 1)]$ is computed from the Lagrangian motion field $[d_{Lx}(x, y, t), d_{Ly}(x, y, t)]$ at time t, and the Eulerian motion field $[d_{Ex}(x, y, t + 1), d_{Ey}(x, y, t + 1)]$ at time $t + 1$ as follows:

$$d_{Lx}(x, y, t + 1) = d_{Lx}(x, y, t) + d_{Ex}(x, y, t + 1), \tag{13}$$

$$d_{Ly}(x, y, t + 1) = d_{Ly}(x, y, t) + d_{Ey}(x, y, t + 1), \tag{14}$$

Myocardial strains can be computed from smooth spatial derivatives of the Lagrangian accumulated motion field $\mathbf{D} = \left[d_{Lx}(x, y, t), d_{Ly}(x, y, t)\right]$ with respect to time. The Green–Lagrange strain tensor is defined as:

$$\mathbf{E} = \frac{1}{2}(\nabla \mathbf{D} + \nabla \mathbf{D}^T + \nabla \mathbf{D}^T \nabla \mathbf{D}), \tag{15}$$

where ∇ is the spatial derivative operator. The vector $\mathbf{D}^T$ stands for the transpose of $\mathbf{D}$. Furthermore, the radial deformation $\mathbf{E}_{\mathrm{rr}}$ and circumferential deformation $\mathbf{E}_{\mathrm{cc}}$ can be obtained by:

$$\mathbf{E}_{\mathrm{rr}} = \mathbf{r}^T \mathbf{E}\mathbf{r}, \mathbf{E}_{\mathrm{cc}} = \mathbf{c}^T \mathbf{E}\mathbf{c}, \tag{16}$$

where $\mathbf{r}$ and $\mathbf{c}$ are the local radial and circumferential directions respectively.

In practice, smooth Gaussian based derivation is used with sigma $= 3.3$, to ensure the tensor map is smooth. However, the quality of myocardial strains requires an accurate estimation of displacement from the cine-MR images.

3. Simulated data and evaluation methods

This section describes the procedure to evaluate the estimated displacement fields from 2D simulated cardiac MRI sequences in the short axis view, including data simulation, mask design, and evaluation metrics.

3.1. Simulated data

The results were tested on several realistic simulated cine cardiac MR image sequences covering a cardiac cycle, in which the benchmark motion was known. Simulated cine-MRI sequences were generated from the realistic warping of a cine MR image using the ASSESS software tool (Clarysse *et al* 2011).

With this simulator, a combination of thickenings and rotations simulate the myocardial contraction over time within a short-axis MRI slice. It is also possible to introduce a local

motion anomaly by reducing the myocardium contraction magnitude within a myocardial sector (Clarysse *et al* 2000). Therefore, the exact displacement at each pixel and time step is known, and is used as a reference to evaluate the proposed method. Several simulations were obtained by acting on the simulator parameters.

In the following, the name of each sequence reflects the values of the parameters used for its generation, namely contraction/expansion (D), rotation (R), frame-rate (F), and healthy (P0), or pathological (P3) state. Several sequences were simulated with increasing motion complexity, ranging from simple thickening to more realistic deformations with and without a local anomaly.

The first simulated cine-MRI had the following parameters: contraction/expansion: 30%, rotation: 20°, frame number: 34, number of systolic time points: 14, number of diastolic time points: 20, image dimensions: 160×160. The sequence was named as D30R20P0F34 where P0 indicates the absence of a contractile anomaly. A sequence with the highest degree of myocardial motion abnormality was also generated (named D30R20P3F34). Two other sequences with 20 frames (end-systole at frame 7) were generated and named D30R20P0F20 and D30R20P3F20, respectively. The displacement field between every pair of neighboring frames in the sequences was computed using our method and two alternative methods (see result section 4).

The noise in magnitude reconstructed MRI images follows a Rician distribution, as demonstrated in Gudbjartsson and Patz (1995) and Cárdenas-Blanco *et al* (2008). In Ding *et al* (2009), Rician noise in the image simulation was introduced by:

$$A = \sqrt{(M + N_{\mathrm{r}})^2 + N_{\mathrm{i}}^2}, \tag{17}$$

where A is the magnitude of image signal corrupted by noise, M is the true image signal, N_{r} and N_{i} are real and imaginary zero-mean Gaussian white noise with identical standard deviation.

When a sequence of frames is available, an idealized description of the image signal intensity I_{n} in the presence of noise in a sequence of K frames is given by

$$I_{\mathrm{n}}(\mathbf{r}, k) = I(\mathbf{r}) + N(\mathbf{r}, k), \tag{18}$$

where $I(\mathbf{r})$ is the original image intensity and $N(\mathbf{r}, k)$ is the additive noise governed by repeated Rician distributions $k = 1 \ldots K$ at position $\mathbf{r} = (x, y)$. For simplicity, we will assume that $N(\mathbf{r}, k)$ is normally distributed in space and time with standard deviation (SD) σ.

A common SNR measurement in the multi-frame case is the $\mathrm{SNR}_{\mathrm{mult}}$ defined as Dietrich *et al* (2007),

$$\mathrm{SNR}_{\mathrm{mult}} = \frac{I_{\mathrm{mult}}}{\sigma_{\mathrm{mult}}} = \frac{\underset{\mathbf{r}\in \mathrm{ROI}, k=1\ldots K}{\mathrm{mean}}(I_{\mathrm{n}}(\mathbf{r}, k))}{\underset{\mathbf{r}\in \mathrm{ROI}, k=1\ldots K}{\mathrm{mean}}(\mathrm{std}(I_{\mathrm{n}}(\mathbf{r}, k)))}, \tag{19}$$

which has no particular requirement on the statistical and spatial distribution of the noise. The functions mean() and std() return the mean and STD values over all pixels within an *ROI* and K repetitions. Here, the ROI is restricted to the LV masks defined in the section 3.2.

The sensitivity of the proposed method to noise was tested and compared with the sensitivity obtained with the Sun (Sun *et al* 2014) and LK methods (Lucas and Kanade 1981). The images in a simulated sequence D30R20P3F20 were normalized from 0 to 255 and corrupted with 3 Rician noise characteristics (σ equals 10, 15 and 20, respectively); those values are commonly used σ values for Rican noise distribution in MRI (Riji *et al* 2014). We named the three sequences as D30R20P3F20_N10, D30R20P3F20_N15, and D30R20P3F20_N20 respectively. These lead to $\mathrm{SNR}_{\mathrm{mult}}$ values of 4.3, 3.1 and 2.6 respectively (see figure 3).

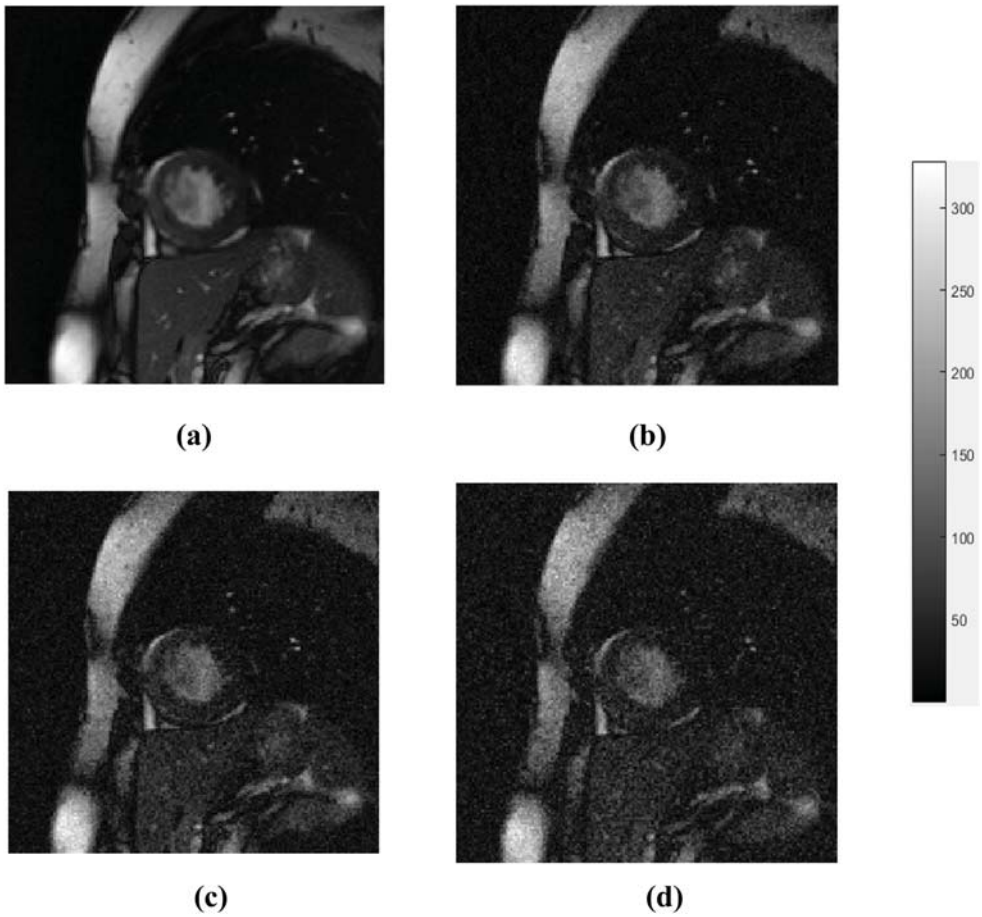

Figure 3. (a) Original cine-MRI image, (b)–(d) corrupted cine-MRI image with Rician noise, standard deviation (STD) equals to 10, 15 and 20, respectively.

3.2. Myocardial region mask

The proposed method provides an estimated displacement field over the whole image domain and cardiac cycle. As our objective is to accurately estimate motion in the myocardium, an image mask was defined where pixels belonging the LV wall were set to 1 and the others to 0. In fact, the mask is predefined as part of the image sequence simulation described in section 3.1; it is an annulus centered in the middle of the cavity in the first frame, and has internal and external radii of 22 and 35 pixels, respectively. It circumscribes the LV myocardium over its course during the whole cardiac cycle (see figure 4).

3.3. Evaluation method

The accuracy of the estimations performed by our method was evaluated against the reference methods using average end-point error (AEE) and average angular error (AAE) statistics. The state-of-the-art Sun algorithm (Sun *et al* 2014), and the Lucas–Kanade algorithm (Lucas and Kanade 1981), were used as the reference methods.

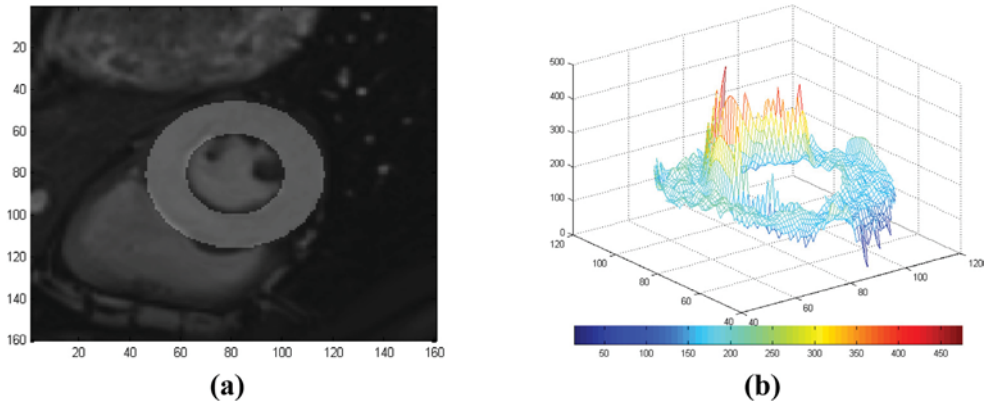

Figure 4. (a) Superimposed ROI (gray region), (b) intensities within the myocardial ROI.

The angular error between two motion vectors, $V_0(\mathbf{p}) = (u_0, v_0)$ and $V_1(\mathbf{p}) = (u_1, v_1)$, at pixel p, is simply defined as the angle between $\mathbf{V}_0$ and $\mathbf{V}_1$ in 2D space

$$\mathrm{AE}(p) = \arccos(\mathbf{v}_0, \mathbf{v}_1), \tag{20}$$

AAE is the average value of AE(p) over the whole LV myocardium for the considered time step. This metric alone, does not take into account large magnitude velocity differences. Therefore, the endpoint error (EE) is introduced as the distance between velocity endpoints (Baker *et al* 2011)

$$\mathrm{EE}(p) = \sqrt{(u_0 - u_1)^2 + (v_0 - v_1)^2}. \tag{21}$$

Average endpoint error (AEE) is the average EE value for all pixels in the LV ROI at a given time step.

In our experiments, both AAE and AEE metrics and their STDs (standard deviations) were used to evaluate the accuracy and stability of the results.

4. Experiments and results

4.1. Results and discussion

Most optical flow methods for cardiac motion analysis are based on tagged-MRI. As myocardium appears homogeneous in cine-MRI, the number of methods discussing dense myocardial motion estimation is low (Wang and Amini 2012). Although incompressible deformable, and registration based methods, could be considered as a reference, they generally require 3D or 4D data.

The performance of our estimator is therefore compared with other reported optical flow methods. The first one is the classical method developed by Lucas and Kanade (1981), and the second is the method developed by Sun *et al* (2010), which makes some improvements, based on the combination of a local and a global method for optical flow assessment. It was declared the best optical flow algorithm in the 2010 Middlebury evaluation ranking (Baker *et al* 2011), and in an expanded literature review in 2014 (Sun *et al* 2014). Hence, this method can be considered as a suitable reference, and will be referred to as the Sun method hereafter.

We used a window size of 11 $\times$ 11 pixels in the LK method. In the Sun method, where the use of median filtering to denoise the flow is the key to improving accuracy, the mask size

Table 1. Mean AEE and AAE ($\mu \pm \sigma$) in pixels over the four noise-free simulated sequences and three noise corrupted simulated sequences.

Sequence Name		Proposed	Sun	LK
D30R20**P3F34**	AEE $\pm$ std	**0.08 $\pm$ 0.05**	0.10 $\pm$ 0.06	0.13 $\pm$ 0.09
	AAE $\pm$ std	**3.59 $\pm$ 2.03**	4.41 $\pm$ 2.59	5.83 $\pm$ 3.98
D30R20**P0F34**	AEE $\pm$ std	**0.07 $\pm$ 0.05**	0.08 $\pm$ 0.05	0.12 $\pm$ 0.11
	AAE $\pm$ std	**3.02 $\pm$ 1.89**	3.36 $\pm$ 2.06	5.06 $\pm$ 5.04
D30R20**P3F20**	AEE $\pm$ std	**0.07 $\pm$ 0.05**	0.11 $\pm$ 0.08	0.16 $\pm$ 0.12
	AAE $\pm$ std	**3.01 $\pm$ 1.88**	4.61 $\pm$ 3.25	7.02 $\pm$ 4.53
D30R20**P0F20**	AEE $\pm$ std	**0.08 $\pm$ 0.06**	0.12 $\pm$ 0.09	0.17 $\pm$ 0.13
	AAE $\pm$ std	**3.41 $\pm$ 2.06**	4.93 $\pm$ 3.09	7.48 $\pm$ 4.55
D30R20**P3F20_N10**	AEE $\pm$ std	**0.23 $\pm$ 0.16**	0.36 $\pm$ 0.20	0.43 $\pm$ 0.27
	AAE $\pm$ std	**9.19 $\pm$ 7.10**	16.33 $\pm$ 9.26	19.69 $\pm$ 9.81
D30R20**P3F20_N15**	AEE $\pm$ std	**0.32 $\pm$ 0.21**	0.48 $\pm$ 0.26	0.50 $\pm$ 0.31
	AAE $\pm$ std	**15.22 $\pm$ 8.50**	22.15 $\pm$ 12.53	23.19 $\pm$ 11.55
D30R20**P3F20_N20**	AEE $\pm$ std	**0.44 $\pm$ 0.25**	0.55 $\pm$ 0.29	0.54 $\pm$ 0.33
	AAE $\pm$ std	**20.38 $\pm$ 12.52**	25.50 $\pm$ 13.29	25.61 $\pm$ 12.43

and neighborhood size were set to 5×5 pixels and 15×15 pixels respectively, to obtain the optimal results on the test sequences in table 1. These parameters were the best suited to our cardiac application.

In our new method, the wavelength and order of the highpass Butterworth filter for the computation of monogenic features were optimized as 5 pixels and 3, respectively. We used a pyramid factor of 0.3 for the coarse to fine multi-resolution strategy, and set the size of the neighborhood to 5×5. We chose a scalar weight of $\varepsilon = 6$ for the optical flow correlation transform.

These values were obtained through a series of tests on the sequences listed in table 1, for which the optimal motion field was known. The methods' parameters were tested in the following ranges: wavelength: 3, 5, 7, 9, and 11 pixels; order of Butterworth filter: 3, 5, and 7; size of the neighborhood: 3×3, 5×5, 7×7 pixels; scalar weight ε: from 3 to 20.

The parameters for all the methods were determined on the basis of the analysis of the sequences in table 1.

All the methods were implemented in MATLAB (R2013a, The Math-Works, Natick, MA, USA), on a desktop computer (CPU: Intel(R) Core(TM) i3-2120 @ 3.3 GHz, RAM: 4.0GB), using Microsoft Windows 7 64 bit operating system.

Table 1 shows the means and standard deviations for AEE and AAE for all three methods and the four noise-free simulated sequences (containing 34 and 20 frames, which are common frame numbers in a cardiac MRI sequence). On the basis of the summation of the AEE and AAE results from the four sequences (D30R20P3F34, D30R20P0F34, D30R20P3F20 and D30R20P0F20), the errors with our proposed method are reduced in comparison with the Sun and LK methods.

As seen from table 1 also, the proposed method is less impacted by Rician noise than the Sun's and LK methods when the noise level σ is in the range 10–15 (sequences N10 and N15). In the sequence with $\sigma = 20$, all the three methods are affected by the noise and have poor performances.

Figures 5(a) and (b) show that the results of the proposed method lead to the smallest end point and angular errors on most frames. For the Lagrangian endpoint errors (figure 5(c)) at the beginning of the systolic phase, the proposed method provides similar performance to

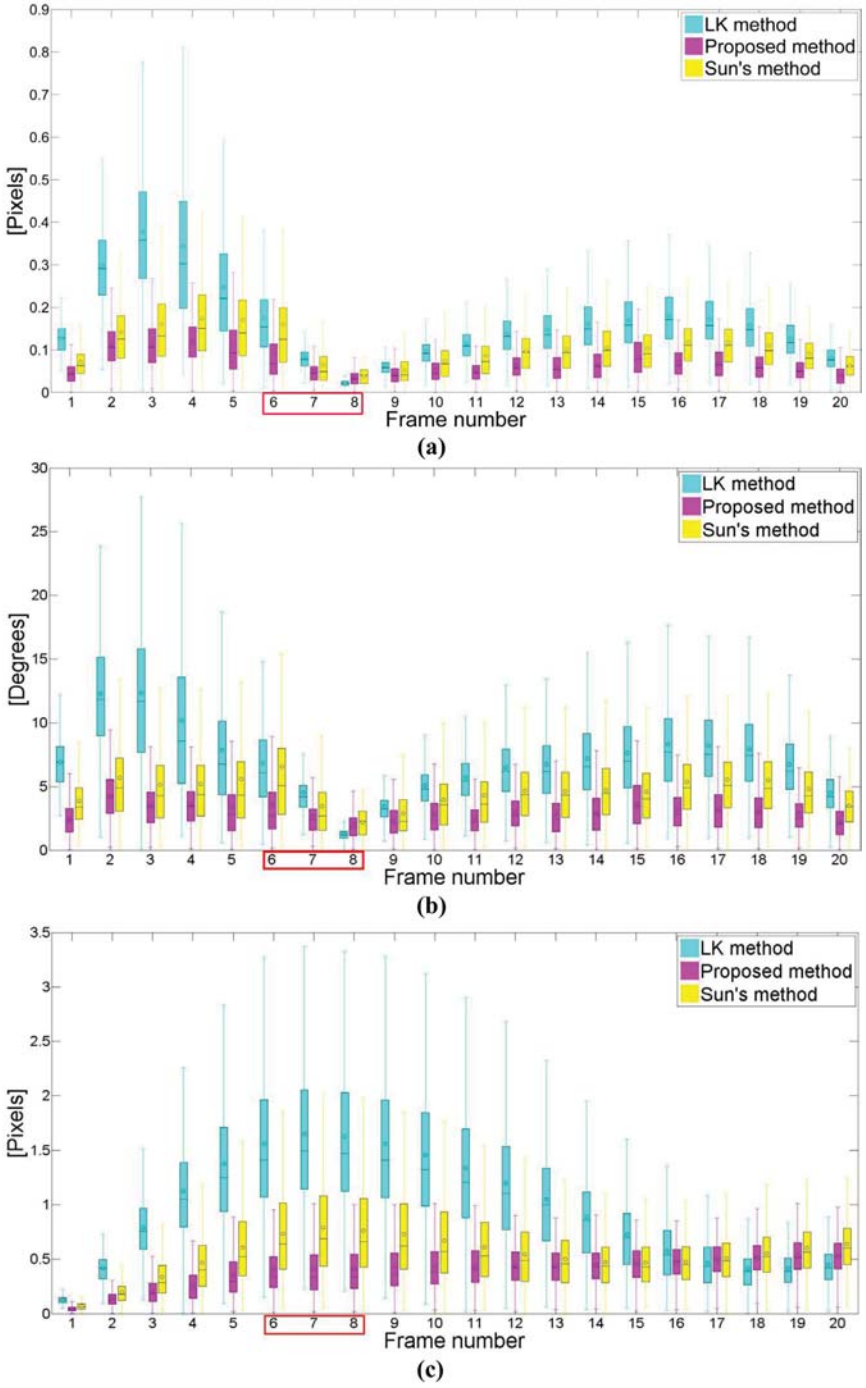

Figure 5. Box and whiskers plots of (a) Eulerian endpoint errors, (b) Eulerian angular errors, and (c) Lagrangian endpoint errors for sequence D30R20P3F20 (with pathology). Frame numbers in the red box correspond to end-systole. Each rectangle corresponds to the statistical distribution of all AEE or AAE values at one frame. The center bar of each box represents the median value. The circle indicates the average value, and the box body extends from the 25th to the75th percentile of one frame of metric values.

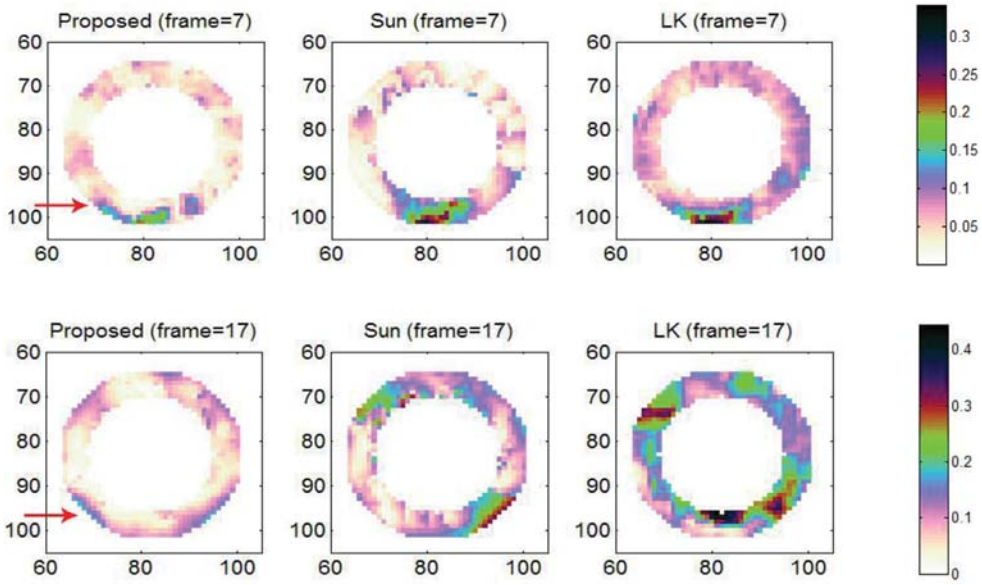

Figure 6. Results of the Eulerian endpoint errors (pixels) for three methods tested on sequence D30R20P3F20 (with pathology). First row: 7th frame close to end-systole; second row: 17th frame close to end-diastole; first column: proposed method; second column: Sun method; third column: LK method. The location of the pathology is indicated by red arrows.

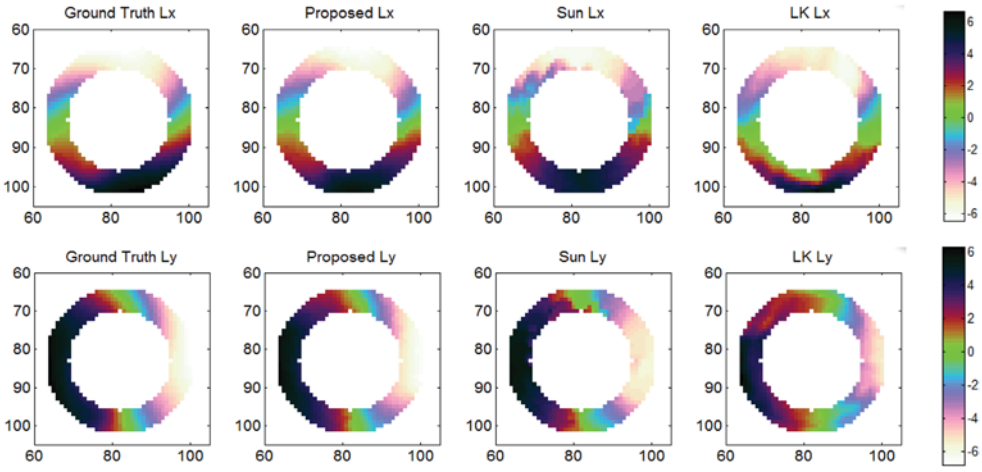

Figure 7. Lagrangian displacement for the sequence D30R20P3F20 (with pathology), at frame #7. First row: Lagrangian displacement in the x direction (Lx); second row: Lagrangian displacement in the y direction (Ly); first column: ground truth; second column: proposed method; third column: Sun method; fourth column: LK method.

the Sun method. From the 1st to 16th frames, the proposed method is more accurate than the other two methods. This is especially the case between the 6th and 10th frames (around end-systole), where the LV expresses a larger deformation, and the proposed method strongly outperforms the Sun method. The LK method, however, performs slightly better at the end of the motion cycle, from the 17th to 20th frames.

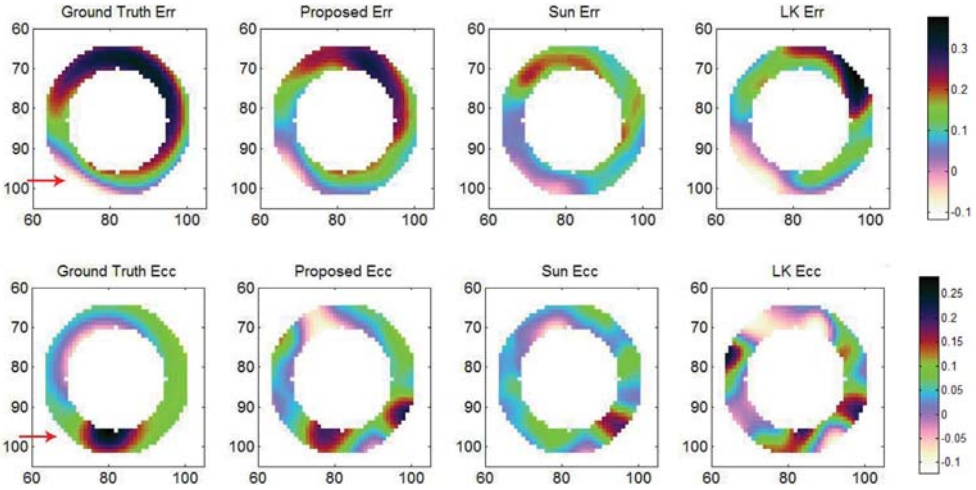

Figure 8. Estimated systolic myocardial strains for the pathological sequence D30R20P3F20 at frame #7 (~end-systole). First row: E_{rr} results; second row: E_{cc} results for the three methods; first column: ground truth; second column: proposed method; third column: Sun method; fourth column: LK method. The location of the pathology is indicated by red arrows.

The results of the Eulerian Endpoint Errors for the three methods applied to sequence D30R20P3F20, at a frame close to end-systole and a frame close to end-diastole, are compared in figure 6. The proposed method resulted in smaller error values, and much smoother maps for both the systolic and diastolic frames.

The Lagrangian displacement results for the three methods at frame #7 (close to end-systole) of sequence D30R20P3F20 are compared in figure 7. The proposed method results in smoother maps, which are more similar to the ground truth map.

Figure 8 shows the radial and circumferential strains for the pathological case in sequence D30R20P3F20 at frame #7 (close to end-systole). A region of simulated pathology is located in the lower left region of the myocardium, indicated by a red arrow.

Radial deformations computed with the three methods are able to highlight the location of the pathology (radial deformations should be mostly positive in systole because of the predominant radial expansion), although the radial deformation from the proposed method is closer to the ground truth data, when compared with the other two methods. Circumferential deformation is, however, not accurately recovered by any of the three methods (circumferential deformations should be mostly negative in systole because of circumferential shortening). This demonstrates the limit of the motion quantification from such images. As can be observed in figure 1(a), the gray level distribution within the myocardial wall of the cine-MR image is quite homogeneous, making the motion estimation problem highly ill-posed. It is therefore most likely that better estimations will be obtained in the radial direction than in the circumferential one, as is the case with the human eye. Recovery of the pathological region from the circumferential strain map is slightly better in our method.

4.2. Analysis of a healthy case and four clinical pathological cases

The analysis of material point trajectories has been discussed previously (Wang *et al* 2015). The motion curves of healthy myocardium are generally longer and more uniform than those in pathological myocardium, while the kinetics in an impaired region are reduced. Most of the negative and weak positive E_{rr} strain values can be detected in the pathological regions.

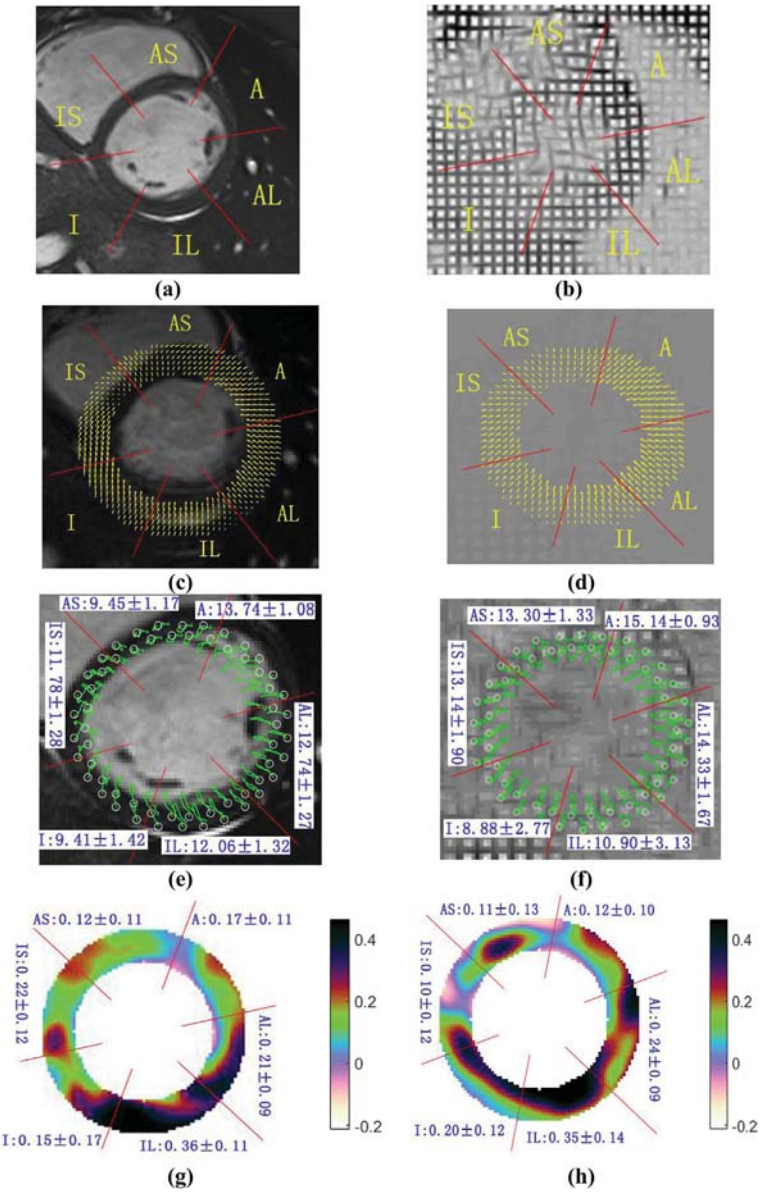

Figure 9. (a) and (b) First frames (end-diastole) of a short-axis cine-MRI sequence and a tagged-MRI sequence for the healthy volunteer. (c) and (d) Lagrangian motion field at end-systolic frame from the cine-MRI sequence and tagged-MRI sequence obtained with the proposed and Wang's methods respectively. (e) and (f) Trace of myocardial point displacements over the whole cine-MRI and tagged-MRI sequences. The mean length $\pm$ the standard deviation of the trajectories for each sector are provided. (g) and (h) Radial strain E_{rr} at end-systole of cine-MRI and tagged-MRI sequences corresponding to contraction maximum. The mean strain values $\pm$ the standard deviation are provided for each standard sector of the myocardium. Sector location is defined as: A = anterior; AS = anteroseptal; IS = inferoseptal; I = inferior; IL = inferolateral; AL = anterolateral. The dysfunctional segments are identified with red labels.

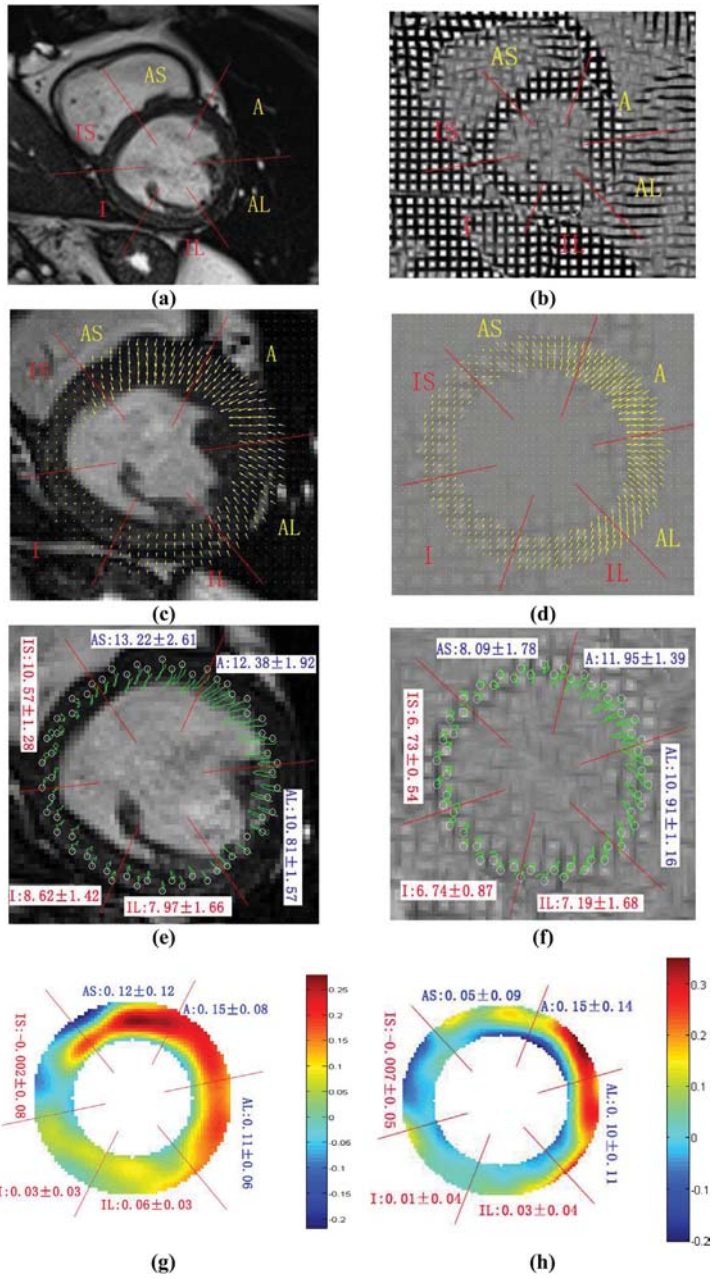

Figure 10. (a) and (b) First frames (end-diastole) of a short-axis cine-MRI sequence and a tagged-MRI sequence for patient #1. (c) and (d) Lagrangian motion field at end-systolic frame from the cine-MRI sequence and tagged-MRI sequence obtained with the proposed and Wang's methods respectively. (e) and (f) Trace of myocardial point displacements over the whole cine-MRI and tagged-MRI sequences. The mean length $\pm$ the standard deviation of the trajectories for each sector are provided. (g) and (h) Radial strain E_{rr} at end-systole of cine-MRI and tagged-MRI sequences corresponding to contraction maximum. The mean strain values $\pm$ the standard deviation are provided for each standard sector of the myocardium.

Table 2. Cine MRI parameters for all clinical cases (1.5T MRI scanner) and dysfunctional segments of pathological cases.

Clinical case names		Sex	Age	TE (ms)	TR (ms)	Flip angle	Spatial resolution (mm)	Frames	Temporal resolution (ms)	Dysfunctional segments
Healthy case		M	44	1.28	49.28	71°	1.17 × 1.17	25	49.28	none
Pathological case	#1	M	64	1.74	38.28	70°	1.5 × 1.5	21	38.28	I, IS, and IL
	#2	M	65	1.74	45.24	70°	1.5 × 1.5	20	45.24	AS, IS, and I
	#3	M	73	1.51	30.2	70°	1.5 × 1.5	21	30.2	I and IL
	#4	F	53	1.51	17.5	70°	1.5 × 1.5	29	17.5	I

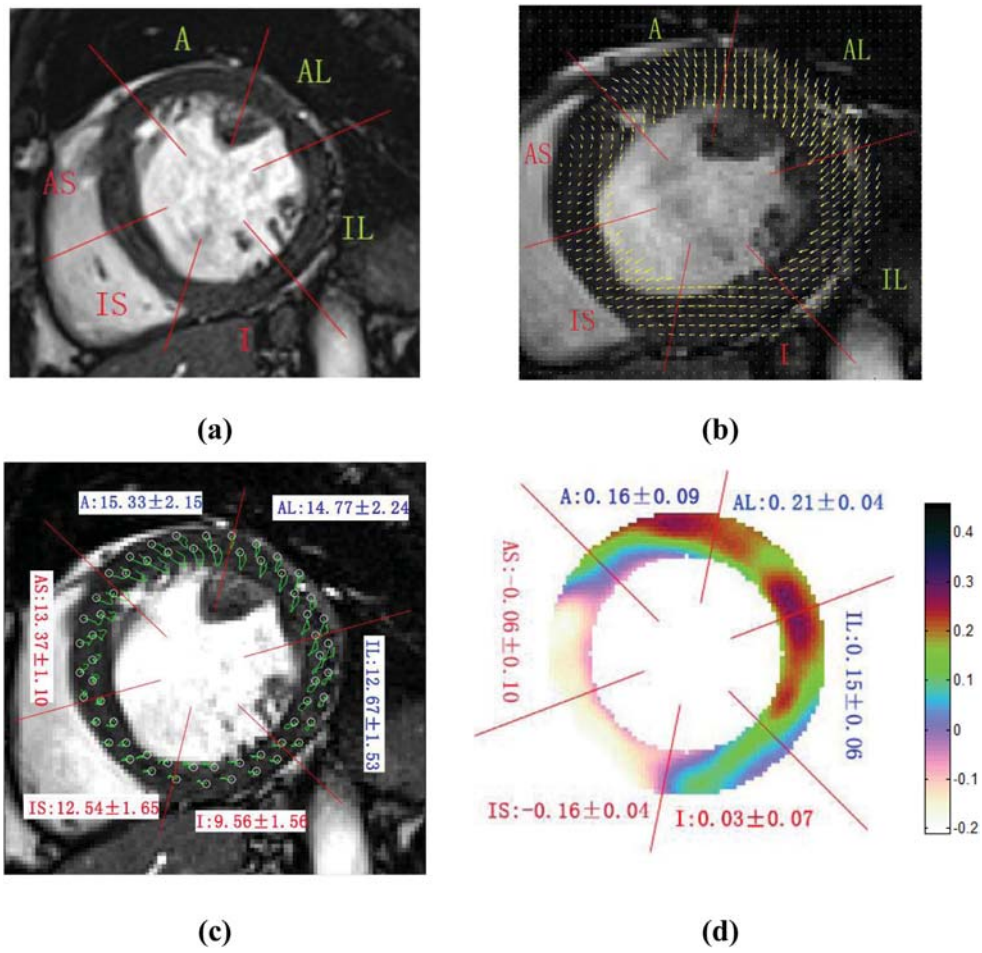

Figure 11. (a) First frame (end-diastole) of a short-axis cine-MRI sequence of patient #2. (b) Lagrangian motion field at an end-systolic frame. (c) Trace of myocardial point displacements over the whole sequence. The mean length ± the standard deviation of the trajectories for each sector are provided (d) radial strain E_{rr} at end-systole for pathological case #2 corresponding to the maximum contraction. The mean strain values ± the standard deviation are provided for each standard sector of the myocardium. The dysfunctional segments are identified with red labels.

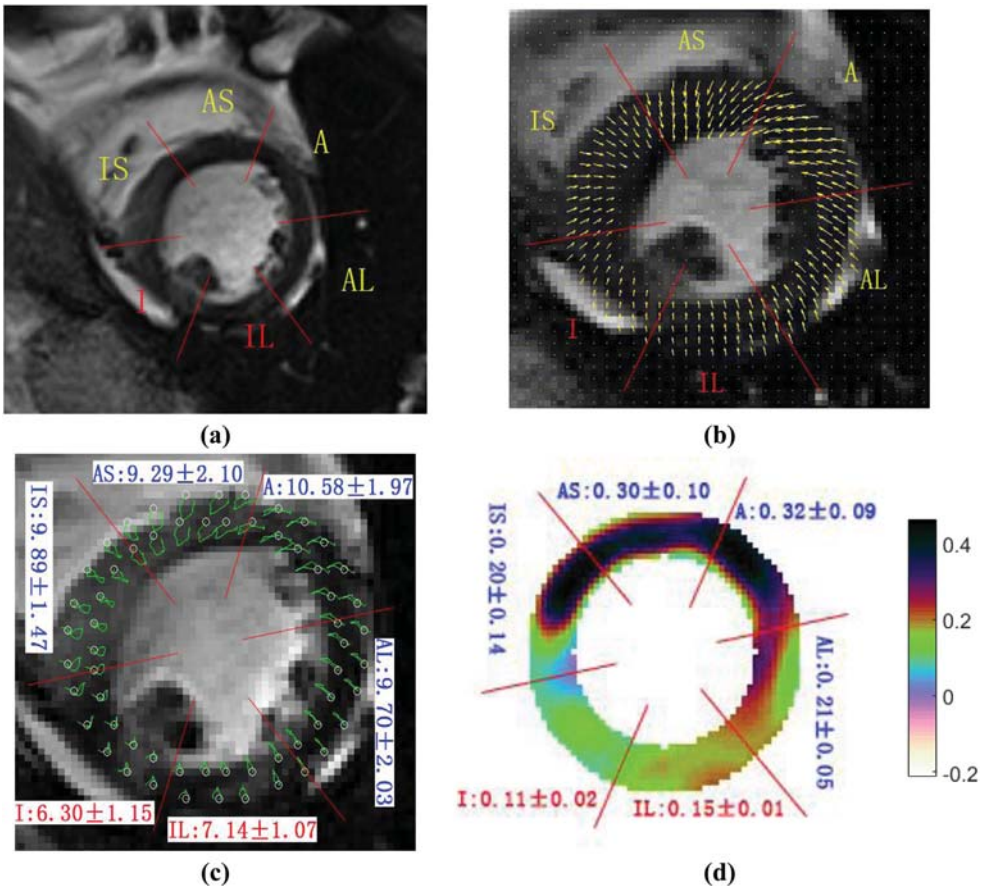

Figure 12. (a) First frame (end-diastole) of a short-axis cine-MRI sequence of patient #3. (b) Lagrangian motion field at an end-systolic frame. (c) Trace of myocardial point displacements over the whole sequence. The mean length ± the standard deviation of the trajectories for each sector are provided (d) radial strain E_{rr} at end-systole for pathological case #3 corresponding to the maximum contraction. The mean strain values ± the standard deviation are provided for each standard sector of the myocardium. The dysfunctional segments are identified with red labels.

For one healthy case and one pathological case, we compared the results obtained with the proposed method applied to a clinical cine-MRI sequence, and those obtained with the Wang's method (Wang *et al* 2015) applied to a clinical tagged-MRI sequence from the same subject. As demonstrated in Wang *et al* (2015), their method performs well in tagged-MRI in comparison with other motion estimators, and is therefore used as a reference for our proposed method. The essential difference between cine-MRI and tagged-MRI is that the latter contains tag patterns that help motion assessment (see figures 9 and 10). For those 2 cases and additional 3 pathological cases, a median short axis (SA) slice were performed in cine MR imaging on a Siemens Avento 1.5T MR scanner. Cine-MRI parameters are given in table 2 for all the cases. An experienced physician diagnosed dysfunctional segments for the pathological cases. Those are also indicated in table 2.

Healthy case: a 44 year-old male healthy volunteer.

First frame of the SA cine sequence is shown in figure 9(a). A tagged MRI sequence of the same volunteer was acquired on a Siemens Avento 1.5T in short-axis views, with the

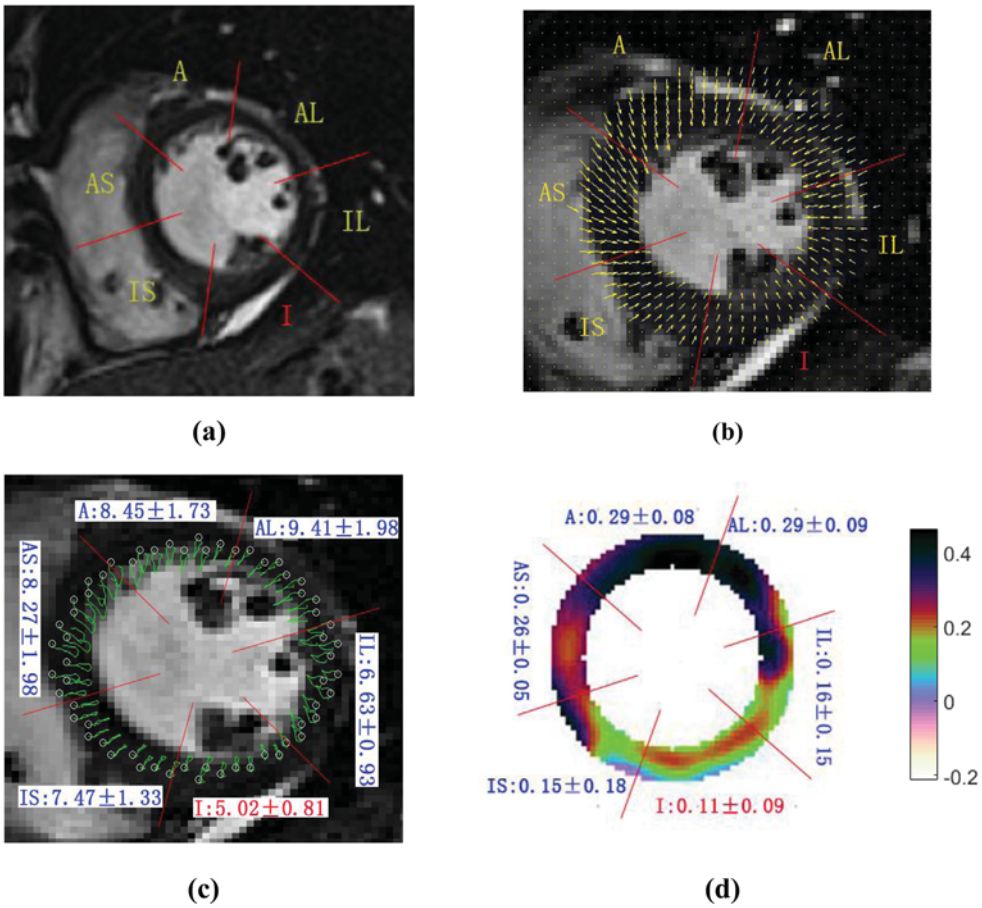

Figure 13. (a) First frame (end-diastole) of a short-axis cine-MRI sequence of patient #4. (b) Lagrangian motion field at an end-systolic frame. (c) Trace of myocardial point displacements over the whole sequence. The mean length ± the standard deviation of the trajectories for each sector are provided (d) radial strain E_{rr} at end-systole for pathological case #4 corresponding to the maximum contraction. The mean strain values ± the standard deviation are provided for each standard sector of the myocardium. The dysfunctional segments are identified with red labels.

following parameters: gradient echo (GRE) sequence with a 45° spatial modulation of magnetization (SPAMM) tagging pattern, TE = 1.23 ms, TR = 34.68 ms, flip angle = 20°, tag spacing = 7 mm, spatial resolution = 1.3 × 1.3 mm, 31 frames, temporal resolution = 34.68 ms. The first frame of this sequence is shown in figure 9(b).

Pathological case #1: a 64 year-old male patient. First frame of the SA cine sequence is shown in figure 10(a). A tagged MRI sequence of the same patient was acquired on a Siemens Avento 1.5T in short-axis views, with the following parameters: GRE sequence with a 45° SPAMM tagging pattern, TE = 1.53 ms, TR = 36.4 ms, flip angle = 20°, tag spacing = 6mm, spatial resolution = 1 × 1 mm, 21 frames, temporal resolution = 36.4 ms.

As shown in figures 9(a)–(h) and 10(a)–(h), similar results at end-systole were obtained for the Lagrangian motion field, trace of the myocardial point displacements, and radial strain E_{rr}, using both the cine and tagged MRI, for both the healthy and the pathological case. The strain maps are formed from displacement fields obtained from the data of cine and tagged images.

In the healthy case, we observe that all the tracked points represent the same tendency (see figure 9), which is different from the motion behavior observed with the pathological case #1 and the additional cases studied hereafter (figures 10–13).

In pathological case #1, the amplitude of the movement in the IS, I, and IL segments (red labels), is visibly smaller than in the other segments, which is in concordance with the location of the pathology (see figures 10(c) and (d)). From the MR based material point trajectories shown in figures 10(e) and (f), a reduced magnitude in the motion of the point trajectory is observed in the IS, I, and IL segments, in accordance with the identified pathological segments. Also, the regions with reduced and negative values in radial strain E_{rr}, shown in figures 10(g) and (h), closely match the location of infarcted segments.

This indicates that the correlation between the Lagrangian motion field, Lagrangian trajectories, and strain images identified in Wang *et al* (2015), also holds for the cardiac motion quantification from cine-MRI analyzed with the method proposed in this study.

Other pathological cases: results obtained for other 3 pathological cases are given in figures 11–13, respectively.

The dysfunctional AS, IS, and I segments in pathological case #2 (figures 11 (a)–(d), red labels), the dysfunctional I and IL segments in pathological case #3 (figures 12(a)–(d), red labels), and the dysfunctional I segment in pathological case #4 (figures 13(a)–(d), red labels) exhibit decreased motion in comparison with the other segments in adjacent or remote myocardium. A reduced motion magnitude and incoherent outward motion direction of the point trajectories can also be observed in these segments, as well as a clear reduction of radial strain E_{rr}.

5. Discussions and conclusion

This work proposes a new method for the quantification of myocardial motion from cine-MRI sequences. It is based on the building of a 3D matrix of monogenic features and a correlation transform of optical flow, inspired by the method introduced by Drulea and Nedevshci (2013). We have adopted an approach to optical flow estimation using zero-mean normalized cross-correlation as a matching measurement. The bilateral filtering acts as a regularization process. The required optimization issue is based on the PPPA strategy.

The results obtained on synthetic data show that the proposed algorithm led to more accurate and smoother motion estimation than that achieved with the standard LK and recent Sun methods. This improvement is mainly due to the introduction of monogenic features into the motion estimation scheme. Synthetic experiments show also a better behavior of the proposed method in the presence of MRI noise.

Preliminary results obtained from cine-MRI sequences from one healthy case and four clinical cases, tend to show that the estimated motion fields obtained with the proposed method are close to the ones obtained using the corresponding tagged-MRI sequences, and can therefore provide reliable myocardial strain estimates that are likely to highlight cardiac motion anomalies. A qualitative analysis of the Lagrangian motion trajectories demonstrated that their shape in pathological sectors was globally different from healthy regions. However, a study on a larger database is necessary to confirm these first findings and constitutes a perspective of this work. Future developments also include the introduction of new texture descriptors and an extension to 3D data.

Acknowledgment

The authors would like to thank the reviewers for their valuable comments. This work was conducted in the framework of the French 3DSTRAIN ANR-11-TecSan-002 project and

LabEX PRIMES (ANR-11-LABX-0063), the National Natural Science Foundation of China (no. 61271092), the Applied Technology Research and Development Program of Heilongjiang Province (no. GC13A311), and the Grant for Science and Innovation Talent of Harbin (2014RFXXJ102).

References

Alessandrini M, Basarab A, Liebgott H and Bernard O 2013 Myocardial motion estimation from medical images using the monogenic signal *IEEE Trans. Image Process.* **22** 1084–95

Amartur S C and Vesselle H J 1993 A new approach to study cardiac motion: the optical flow of cine MR images *Magn. Reson. Med.* **29** 59–67

Augustine D *et al* 2013 Global and regional left ventricular myocardial deformation measures by magnetic resonance feature tracking in healthy volunteers: comparison with tagging and relevance of gender *J. Cardiovasc. Magn. Reson.* **15** 8

Axel L and Dougherty L 1989 Heart wall motion: improved method of spatial modulation of magnetization for MR imaging *Radiology* **172** 349–50

Axel L, Montillo A and Kim D 2005 Tagged magnetic resonance imaging of the heart: a survey *Med. Image Anal.* **9** 376–93

Baker S, Scharstein D, Lewis J P, Roth S, Black M J and Szeliski R 2011 A database and evaluation methodology for optical flow *Int. J. Comput. Vision.* **92** 1–31

Cárdenas-Blanco A, Tejos C, Irarrazaval P and Cameron I 2008 Noise in magnitude magnetic resonance images *Concepts Magn. Reson.* A **32A** 409–16

Chambolle A and Pock T 2011 A first-order primal-dual algorithm for convex problems with applications to imaging *J. Math. Imaging Vis.* **40** 120–45

Clarysse P, Basset C, Khouas L, Croisille P, Friboulet D, Odet C and Magnin I E 2000 Two-dimensional spatial and temporal displacement and deformation field fitting from cardiac magnetic resonance tagging *Med. Image Anal.* **4** 253–68

Clarysse P, Tafazzoli J, Delachartre P and Croisille P 2011 Simulation based evaluation of cardiac motion estimation methods in tagged-MR Image sequences *J. Cardiovasc. Magn. Reson.* **13** 360

Cowan B R, Peereboom S M, Greiser A, Guehring J and Young A A 2015 Image feature determinants of global and segmental circumferential ventricular strain from cine CMR *JACC Cardiovasc. Imaging* **8** 1465–6

D'Hooge J, Heimdal A, Jamal F, Kukulski T, Bijnens B, Rademakers F, Hatle L, Suetens P and Sutherland G R 2000 Regional strain and strain rate measurements by cardiac ultrasound: principles, implementation and limitations *Eur. J. Echocardiogr.* **1** 154–70

Di Stefano L, Mattoccia S and Tombari F 2005 ZNCC-based template matching using bounded partial correlation *Pattern Recognit. Lett.* **26** 2129–34

Dietrich O, Raya J G, Reeder S B, Reiser M F and Schoenberg S O 2007 Measurement of signal-to-noise ratios in MR images: influence of multichannel coils, parallel imaging, and reconstruction filters *J. Magn. Reson. Imaging* **26** 375–85

Ding Y, Chung Y C, Raman S V and Simonetti O P 2009 Application of the Karhunen–Loeve transform temporal image filter to reduce noise in real-time cardiac cine MRI *Phys. Med. Biol.* **54** 3909–22

Drulea M and Nedevschi S 2013 Motion estimation using the correlation transform *IEEE Trans. Image Process.* **22** 3260–70

Felsberg M 2007 Optical flow estimation from monogenic phase *Complex Motion* (Berlin: Springer) pp 1–13

Felsberg M and Sommer G 2001 The monogenic signal *IEEE Trans. Signal Process.* **49** 3136–44

Gorce J-M, Friboulet D and Magnin I E 1997 Estimation of three-dimensional cardiac velocity fields: assessment of a differential method and application to three-dimensional CT data *Med. Image Anal.* **1** 245–61

Gudbjartsson H and Patz S 1995 The Rician distribution of noisy MRI data *Magn. Reson. Med.* **34** 910–4

He B S and Yuan X M 2012 Convergence analysis of primal-dual algorithms for a saddle-point problem: from contraction perspective *SIAM J. Imaging Sci.* **5** 119–49

Hor K N *et al* 2010 Comparison of magnetic resonance feature tracking for strain calculation with harmonic phase imaging analysis *JACC Cardiovasc. Imaging* **3** 144–51

Horn B K and Schunck B G 1981 Determining optical flow *Artif. Intell.* **17** 185–203
Kuetting D, Sprinkart A M, Doerner J, Schild H and Thomas D 2015 Comparison of magnetic resonance feature tracking with harmonic phase imaging analysis (CSPAMM) for assessment of global and regional diastolic function *Eur. J. Radiol.* **84** 100–7
Lamacie M M, Thavendiranathan P, Hanneman K, Greiser A, Jolly M P, Ward R and Wintersperger B J 2016 Quantification of global myocardial function by cine MRI deformable registration-based analysis: comparison with MR feature tracking and speckle-tracking echocardiography *Eur. Radiol.* (doi:10.1007/s00330-016-4514-0)
Lin C H, Tsai J S and Chiu C T 2010 Switching bilateral filter with a texture/noise detector for universal noise removal *IEEE Trans. Image Process.* **19** 2307–20
Lucas B D and Kanade T 1981 An iterative image registration technique with an application to stereo vision *Proc. of the 7th Int. Joint Conf. on Artificial Intelligence* pp 674–9
Okutomi M and Kanade T 1992 A locally adaptive window for signal matching *Int. J. Comput. Vision* **7** 143–62
Oubel E, De Craene M, Hero A O, Pourmorteza A, Huguet M, Avegliano G, Bijnens B H and Frangi A F 2012 Cardiac motion estimation by joint alignment of tagged MRI sequences *Med. Image Anal.* **16** 339–50
Qian Z, Liu Q S, Metaxas D N and Axel L 2011 Identifying regional cardiac abnormalities from myocardial strains using nontracking-based strain estimation and spatio-temporal tensor analysis *IEEE Trans. Med. Imaging* **30** 2017–29
Riji R, Rajan J, Sijbers J and Nair M S 2014 Iterative bilateral filter for Rician noise reduction in MR images *Signal Image Video Process.* **9** 1543–8
Sadeghpour A 2013 Myocardial strain and strain rate imaging: comparison between doppler derived strain imaging and speckle tracking echocardiography *Arch. Cardiovasc. Imaging* **1** 20–1
Sun D, Roth S and Black M J 2010 Secrets of optical flow estimation and their principles *IEEE Conf. on Computer Vision and Pattern Recognition* pp 2432–9
Sun D Q, Roth S and Black M J 2014 A quantitative analysis of current practices in optical flow estimation and the principles behind them *Int. J. Comput. Vis.* **106** 115–37
Tomasi C and Manduchi R 1998 Bilateral filtering for gray and color images *IEEE 6th Int. Conf. on Computer Vision* pp 839–46
Wang H and Amini A A 2012 Cardiac motion and deformation recovery from MRI: a review *IEEE Trans. Med. Imaging* **31** 487–503
Wang L, Basarab A, Girard P R, Croisille P, Clarysse P and Delachartre P 2015 Analytic signal phase-based myocardial motion estimation in tagged MRI sequences by a bilinear model and motion compensation *Med. Image Anal.* **24** 149–62
Wedel A, Pock T, Zach C, Bischof H and Cremers D 2009 An improved algorithm for TV-L1 optical flow *Statistical and Geometrical Approaches to Visual Motion Analysis* (*Lecture Notes in Computer Science* vol 5604) (Berlin: Springer) pp 23–45
Werys K, Vijayakumar S, Ranjan R, Dosdall D J, Kim D, Marrouche N F and Kholmovski E 2013 CINE-MRI to study the progress of disease in a chronic atrial fibrillation goat model *J. Cardiovasc. Magn. Reson.* **15** E96
White R D, Obuchowski N A, Gunawardena S, Lipchik E O, Lever H M, Van Dyke C and Lytle B W 1996 Left ventricular outflow tract obstruction in hypertrophic cardiomyopathy: presurgical and postsurgical evaluation by computed tomography magnetic resonance imaging *Am. J. Card. Imaging* **10** 1–13 (PMID: 8680128)
Wu L, Germans T, Guclu A, Heymans M W, Allaart C P and van Rossum A C 2014 Feature tracking compared with tissue tagging measurements of segmental strain by cardiovascular magnetic resonance *J. Cardiovasc. Magn. Reson.* **16** 10
Xavier M, Lalande A, Walker P M, Brunotte F and Legrand L 2012 An adapted optical flow algorithm for robust quantification of cardiac wall motion from standard cine-MR examinations *IEEE Trans. Inf. Technol. Biomed.* **16** 859–68
Xia F Q and Huang N J 2011 A projection-proximal point algorithm for solving generalized variational inequalities *J. Optim. Theory Appl.* **150** 98–117
Yang J, Agterberg F P and Cheng Q M 2015 A novel filtering technique for enhancing mineralization associated geochemical and geophysical anomalies *Comput. Geosci.* **79** 94–104
Zerhouni E A, Parish D M, Rogers W J, Yang A and Shapiro E P 1988 Human heart: tagging with MR imaging—a method for noninvasive assessment of myocardial motion *Radiology* **169** 59–63
Zhang M and Gunturk B K 2008 Multiresolution bilateral filtering for image denoising *IEEE Trans. Image Process.* **17** 2324–33